Electronic Supplementary Material (ESI) for Physical Chemistry Chemical Physics.

Supplementary Information
A Thermostated Cell for Electrochemistry: Minimising Natural Convection and Investigating the Role of Evaporation and Radiation

Xiuting Li[+], Christopher Batchelor-McAuley[+], Javor K. Novev[+] and Richard G. Compton*

* corresponding author: Richard G. Compton, Department of Chemistry, Physical & Theoretical Chemistry Laboratory, Oxford University, South Parks Road, Oxford, OX1 3QZ, United Kingdom

Email: richard.compton@chem.ox.ac.uk. Tel: +44(0)1865275 957 Fax: +44(0)1865275410

[+] These authors contributed equally to this work.

Table of Contents

Section 1. Assessment of the importance of the Marangoni effect

In general, the right-hand side of the tangential stress balance (11) contains the gradient of the surface tension γ, $d\gamma/dr = \partial_T\gamma \cdot \partial_r T^L\big|_{z = h_{liquid} + d_{wall}}$, which could potentially drive a Marangoni flow[1]. Marangoni flows are not considered here in the interest of simplicity; moreover, as previous studies on similar topics have shown, the thermal Marangoni effect that the radial temperature gradient at $z = h_{liquid} + d_{wall}$ induces can be completely suppressed in the presence of a surface-active contaminant; in Hu and Larson[2] have demonstrated that for an evaporating sessile droplet, this happens at adsorptions as low as $5\text{x}10^{-10}$ mol·m^{-2}. Furthermore, Marangoni flows typically dominate in thin layers[1] rather than enclosures such as ours whose vertical and lateral dimensions are similar. The relative contributions of the surface-tension and buoyancy-driven flows can be assessed by calculating the dimensionless criteria controlling the two, respectively the Marangoni and Rayleigh numbers, $Ma = |\partial_T\gamma|h_{liquid}|\Delta T|/\left(\eta_0\chi^L\right)$ and $Ra = \left(\rho_0^L\alpha h_{liquid}^{\ 3}|\Delta T||g|\right)/\left(\chi^L\eta_0\right)$. The ratio between them quantifies the relative importance of the two effects, see e.g. Keller and Bergman[3] and its low value, $Ma/Ra = |\partial_T\gamma|/\left(\rho_0^L\alpha h_{liquid}^{\ 2}|g|\right) \approx 0.11$ (consult SI2 for values of the parameters), justifies neglecting the Marangoni flow.

Section 2. Details of the simulation procedure

For the density, thermal conductivity and heat capacity of glass, the approximate values $\rho_{\text{glass}} = 2.2\text{x}10^3$ kg·m^{-3}, $\kappa_{\text{glass}} = 1.14$ W·m^{-1}·K^{-1} and $C_{p\,\text{glass}} = 830$ J·kg^{-1}·K^{-1} have been used. The parameters of the liquid are taken at $T_{\text{solution }0}$ and calculated as follows: the density ρ_0^L and the thermal expansion coefficient α are calculated from eq. 16 in Ref.[4]; the heat capacity C_p^L is taken from eq. 17 in the same reference; the viscosity η is computed from eq. 15 in Ref. [5] and the heat conductivity κ – from eq. 10 in Ref. [6]. For calculating the Marangoni number, the value of the temperature derivative of surface tension of water measured by Cini et al.[7] at 293.15 K, $\partial_T\gamma = -0.149\ mN \cdot m^{-1} \cdot K^{-1}$ was used.

The simulations of the heat transfer in the cell were conducted in COMSOL Multiphysics® 5.3. A free triangular mesh was used for the bulk of the fluid and the cell; the regions next to the no-slip surfaces and the liquid|gas interface were meshed with 5 boundary layers; the total number of mesh elements used was 15317. The temporal discretization was performed with a maximum time-step of 0.5 s. To ensure convergence had been achieved, the simulations were repeated with a finer mesh having 10 boundary layers next to the no-slip and the liquid|gas interfaces and consisting of 33690 elements; the maximum time step was reduced to 0.25 s. The results for $\Delta T_{\text{probe}} = T_{\text{thermostat}} - T_{\text{probe}}$ were compared between the two types of simulations and found to agree within 1.3% across the whole time domain of the study.

Section 3. Assessment of the experimental significance of the perturbations in $\Delta T_{\mathrm{probe}}$ at short times

The following analysis aims to determine whether the thermometer probe used in the experiments conducted here can measure the perturbations in $\Delta T_{\mathrm{probe}}$ predicted by simulations with free-surface boundary conditions. To this end, the probe was subjected to an approximate square-wave temperature disturbance – after having been equilibrated with the surrounding air at $T \sim 295.3$ K, it was immersed in water with a temperature of $T \sim 297.9$ K. The probe's response was monitored and modelled as that of a first-order low-pass Butterworth filter with a cut-off frequency of 0.175 Hz, chosen so that filtering a square-pulse disturbance of similar amplitude, $T - T(t = 0) = 2.6 \cdot \eta(t - 5)\eta(20 - t)$, η being the Heaviside step function, yielded a result comparable to the experimental data (see Figure S. 1).

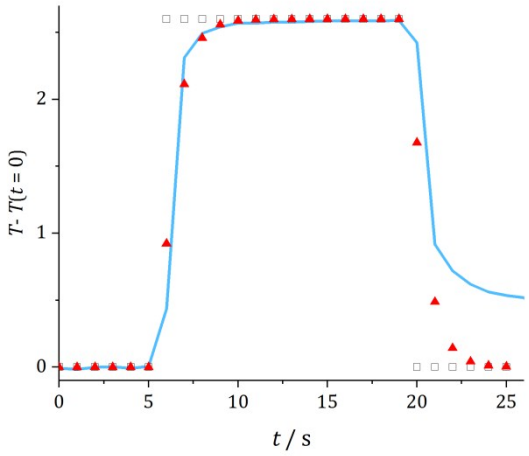

Figure S.1. Test of the response time of the thermometer probe. Solid line – recorded response of the sensor upon its immersion in water; squares – simulated square pulse; triangles – square wave filtered with a first-order low-pass Butterworth filter with a cut-off frequency of 0.175 Hz.

This filter was then used to process simulated data for $T_{\mathrm{probe}} - T_{\mathrm{solution}\ 0} = \Delta T - \Delta T_{\mathrm{probe}}$ for simulations of sealed cells with radiative heat flux, free-surface and no-slip boundary conditions and ΔT 1.3 and 1.8 K sampled with a frequency of 1 Hz; the results are plotted in Figure S. 2. As the figure, which deals with the same data as Figure 2B from the main text and Figure S. 3B, indicates, the probe's response time would allow it to record disturbances such as those predicted for $\Delta T_{\mathrm{probe}}$ for free-surface conditions. Thus, the fact that such disturbances were not observed in the experimental data is a strong indication that a no-slip rather than a free surface boundary condition is appropriate for the system.

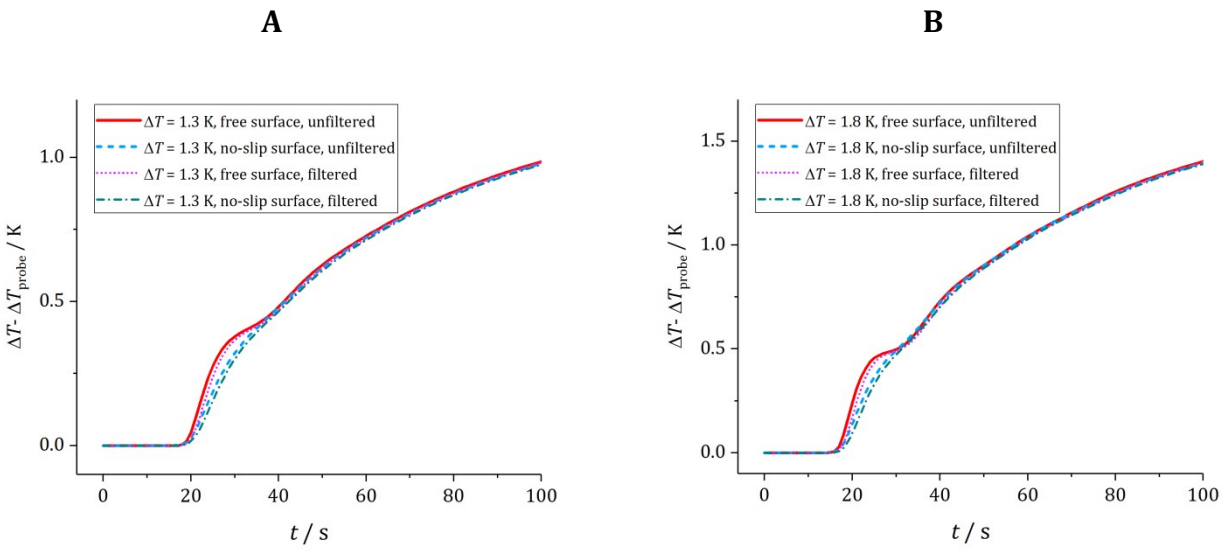

Figure S.2. Data for $T_{probe} - T_{solution\ 0}$ at **A**) ΔT = 1.3 K and **B**) ΔT = 1.8 K from simulations with 1) no filtering and a free-surface boundary condition (solid lines) or a no-slip boundary condition (dashed lines); 2) data from free-surface (dotted lines) and no-slip (dash-dot lines) filtered with a first-order Butterworth filter with a cut-off frequency of 0.175 Hz. Although the filter induces a time-delay and alters the data, there is still a significant difference between the cases of free and no-slip hydrodynamic boundary conditions. This implies that the thermometer probe is capable of measuring such perturbations and, as fluctuations such as the ones seen here for the free-surface case are not seen experimentally, is an argument in favour of employing a no-slip boundary condition.

Section 4. Data for simulations and experiments at ΔT = 1.8 K

Figure S. 3 presents data from simulations and experiments at ΔT = 1.8 K; it is equivalent to Figure 2 from the main text but presents a case with a larger initial temperature difference.

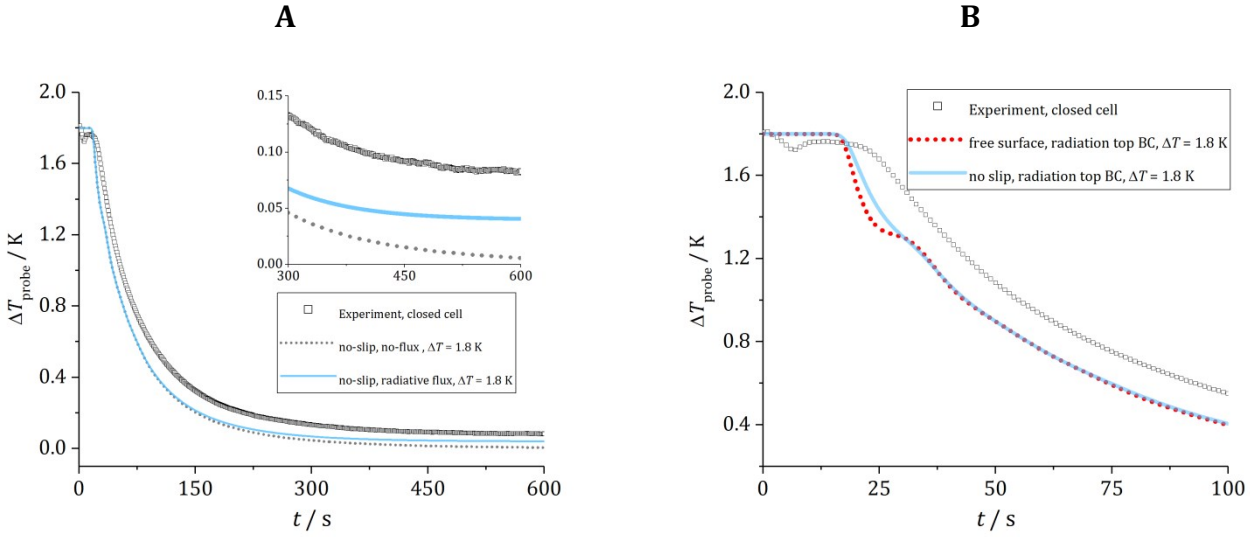

Figure S.3. Difference between the temperature of the thermostat and that at the measurement point as a function of time at an initial ΔT of 1.8 K. **A**. Comparison of experimental data (points) and simulations with a no-slip boundary having 1) a no-flux boundary condition (dashed line) and 2) a radiative heat flux condition at the liquid|air interface (solid line). Note that the simulation with a boundary condition for thermal insulation predicts that the solution temperature asymptotically tends towards $T_{thermostat}$, whereas the one with radiative heat flux predicts a temperature difference close to the experimentally observed one. **B**. Plot of the experimental data from **A** at short times and calculated values for simulations with radiative heat flux, 1) a no-slip hydrodynamic boundary condition (solid line) and 2) a free-surface one (dashed line).

Figure S. 4 presents the evolution of the temperature and velocity fields for a simulation with free surface boundary conditions and radiative heat transfer at ΔT = 1.8 K. As discussed in the main text, the greater driving force for the convection yields a considerable difference in the observed flow – here, the intensity of the secondary roll that develops close to the cylinder axis is large enough to significantly perturb the temperature profile in the vicinity of the substrate, as seen in Figure S. 4C. As in the case with a smaller initial temperature difference, the two convective cells merge at long times and a single roll occupies the whole volume of the liquid.

The provided supplementary animations illustrate the evolution of the flows for several simulations more completely. Two types of animations are provided – 1) $T_{thermostat} - T$ overlaid with streamlines and an arrow plot of $\boldsymbol{v}$ and 2) $|\boldsymbol{v}|$, again overlaid with streamlines and an arrow plot of $\boldsymbol{v}$. Such plots are provided for the simulations with no-slip hydrodynamic boundary conditions at the liquid|gas interface at ΔT = 1.3 and 1.8 K.

In simulations conducted with ΔT = 2.3, the secondary flow intensifies and $\Delta T_{probe}(t)$ goes through five inflections. In simulations with ΔT = 3 and 4 K, it is observed that the vertically elongated secondary flows become considerably more pronounced and so does their influence on ΔT_{probe}, causing the simulated curve to have not just multiple inflections but also multiple extrema. As the experimentally measured T_{probe} does not possess such features, the discussion is restricted of the flow patterns to the

case with $\Delta T \leq 2.3$ K in which the secondary convective cells have only a limited effect. It should be noted that as part of the study, convective flow patterns qualitatively similar to the predicted ones have been experimentally observed at $\Delta T \approx 7$ K via monitoring the dissolution of a $KMnO_4$ crystal placed at its bottom.

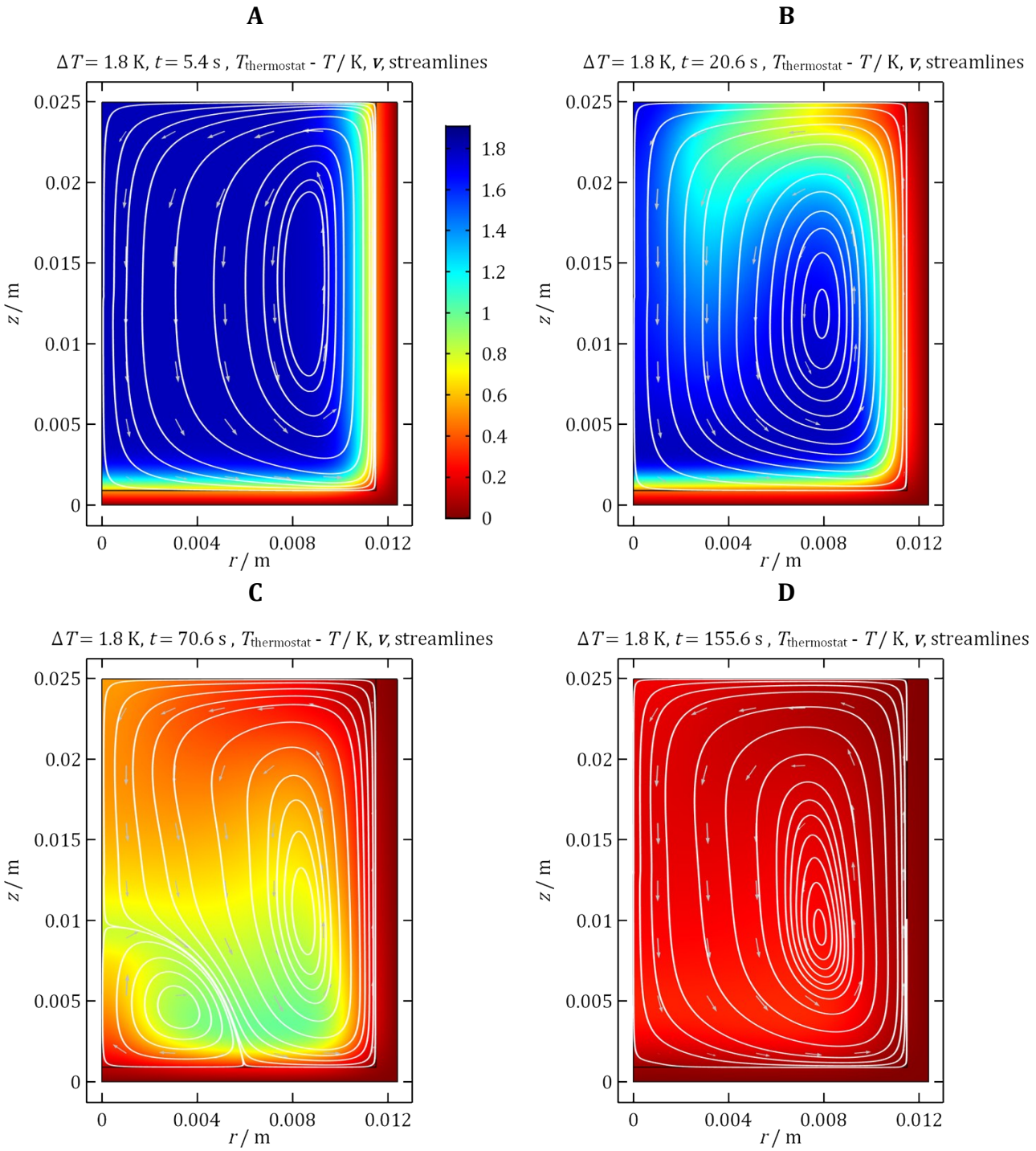

Figure S.4. Temperature distribution, streamlines and arrow plot of the velocity field for a simulation with a no-slip surface, a boundary condition for radiative heat transfer through the liquid|gas interface and ΔT = 1.8 K. In each plot, the length of the arrows is proportional to the local value of $|\boldsymbol{v}|$, but the proportionality constant varies between frames. Note that in this case the secondary roll that appears at the cylinder axis is of substantial intensity and perturbs the local temperature profile to a much greater degree than at ΔT = 1.3 K, compare **C** with Figure 3**C** in the main text.

Section 5. Additional data for simulations and experiments at ΔT = 2.3 K

Figure S. 5 contains a comparison of the simulated ΔT_{probe} curves from Figure 4 in the main text with ones that involve no evaporative heat flux. As in Figure 4, where results for a closed cell are illustrated, for such simulations ΔT_{probe} tends towards zero at long times if a no-flux boundary condition is imposed at the liquid|gas interface and towards 0.04 K if radiative flux is assumed. The inset in Figure S. 5A demonstrates that such temperature differences are considerably smaller than the experimentally observed ones, suggesting that evaporation plays a significant role in this system.

Figure S. 5B presents the same data as Figure S. 5A but focuses on the region of short times, showcasing the small maximum in ΔT_{probe} that simulations with an evaporative flux predict. Moreover, it is seen from Figure S. 5B that both simulations with evaporation yield identical ΔT_{probe} at short times – this happens because the radiative heat flux only becomes important towards the end of the experiment when the temperature difference between the solution and the ambient air is at its largest.

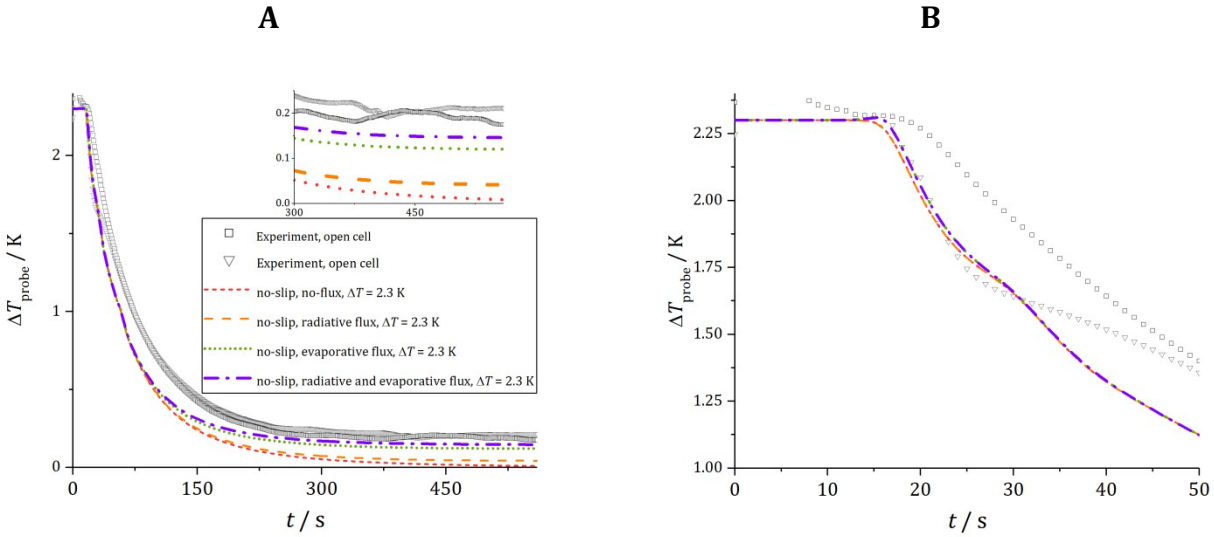

Figure S.5. Difference between the temperature of the thermostat and that at the measurement point as a function of time at an initial ΔT of 2.3 K. The two sets of points correspond to experimental measurements for a cell open to the environment. Points at short t are not shown as they deviate strongly from the trend because when the cell is placed in the water bath, the thermometer probe is exposed to the air. The curves represent simulations with a no-slip surface and different thermal boundary conditions at the liquid|gas interface: 1) no flux (short-dashed line), 2) radiation heat flux (long–dashed line), 3) evaporative heat flux (dotted line) and 4) radiation and evaporative heat flux (dash-dot line). The simulation that includes both evaporative and radiative heat transfer is in closest agreement with the experimental data, which suggests that the model including these two mechanisms for heat exchange is the most adequate for an open cell.

Section 6. Data on ΔT_{probe} for a cell immersed deeper in the water bath

Figure S.6 illustrates measurements for ΔT_{probe} conducted with a cell of greater height that is positioned deeper within the water bath than for the other experiments discussed in the paper. The simulated curves correspond to boundary conditions for a no-slip surface combined with either a thermal insulation or a radiation condition at the liquid|gas interface for the heat transfer problem. As discussed in the main text, performing the experiment under such conditions leads to better agreement with simulations at long times, suggesting that contrary to the assumption of the model, the temperature distribution in the water bath is not homogeneous. However, the agreement between data for the smaller cell and our simulations is both sufficiently good for the purpose of this study and more relevant to the cell for nano-impacts, so more detailed studies of the alternative experimental configuration have not been performed.

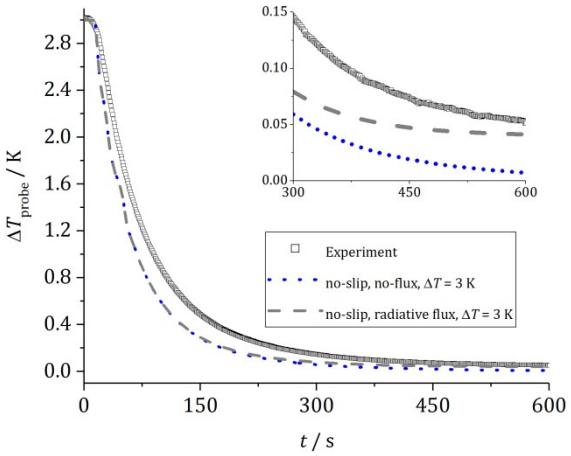

Figure S.6. Difference between the temperature of the thermostat and that at the measurement point as a function of time at an initial ΔT of 3 K. The curves are determined experimentally for a sealed cell that is fully immersed in the water bath (squares), from simulations with a no-slip surface having 1) a no-flux boundary condition (dotted line) and from 2) a boundary condition for radiative heat transfer (dashed line). Note that the simulation with an insulation boundary condition predicts that the solution temperature asymptotically tends towards $T_{\text{thermostat}}$, whereas the one with radiative heat flux predicts a temperature difference similar to the experimentally observed one.

Section 7. Volume-averaged velocities of the observed flows

Figures S.1-1 present the volume-averaged velocity $|\boldsymbol{v}_{av}|$ as defined by eq. (13) for various simulations; for all of them, $|\boldsymbol{v}_{av}|$ goes through a sharp maximum corresponding to the period of most intense flow before the temperature difference between the solution and the thermostat has diminished. The position and height of this peak depend on the initial temperature difference ΔT, as the comparison between simulations with ΔT = 1.3 (solid, dashed and dotted lines) and 1.8 K (dashdot line) in Figures S.1 shows. Moreover, it is visible from Figure S.1 that while a free-surface boundary condition leads to a higher maximum average velocity, this effect is minor – the latter condition leads to $|\boldsymbol{v}_{av}|_{max}$ = 8.0x10^{-4} m·s^{-1} at ΔT = 1.3 K, which is close to the value of 7.7x10^{-4} m·s^{-1} for a no-slip surface at the same initial temperature difference. Furthermore, Figure S.1 illustrates that, crucially, if the heat flux through the liquid|gas interface is neglected, $|\boldsymbol{v}_{av}|$ tends to zero at long times, reaching 7.5x10^{-6} m·s^{-1} at t_{exp} for a simulation with ΔT = 1.3 K – in this case, the system tends to an equilibrium state with a homogeneous temperature distribution. In contrast, when a radiative heat flux condition is imposed at the surface, the temperature distribution remains inhomogeneous even at long times, thus providing a driving force for convection and leading to an average velocity $|v_{av}|_{t\,=\,t_{exp}} \approx$ 6.6x10^{-5} and 6.5x10^{-5} m·s^{-1} for no-slip hydrodynamic boundary conditions at ΔT = 1.3 and 1.8 K. A likely explanation for the difference between the $|v_{av}|_{t\,=\,t_{exp}}$ between simulations at different initial ΔT is that a true stationary state is not yet reached at this point in time.

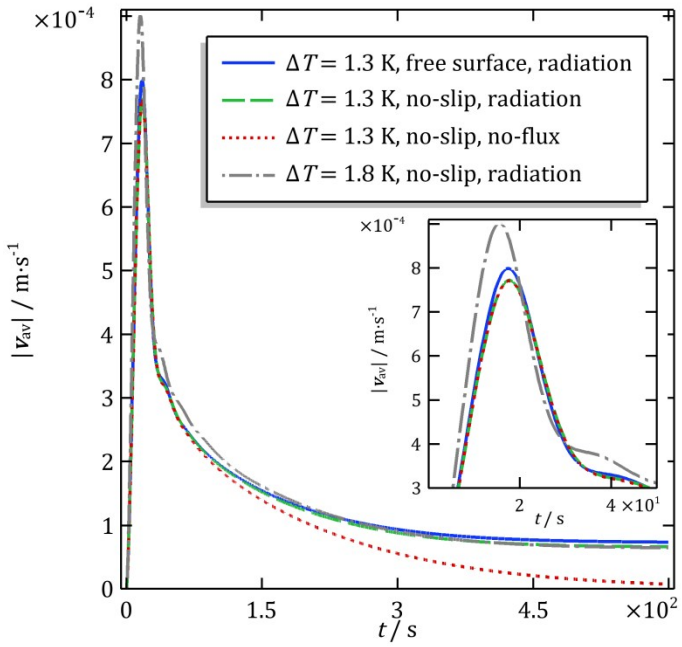

Figure S.7. Comparison of the volume-averaged velocity magnitude for four different simulations of closed-cell systems. Curves represent simulations with the following types of boundary conditions at the liquid|gas interface at ΔT = 1.3 K: solid – free-surface boundary and a radiation heat flux; dashed – no-slip and a radiation heat flux; dotted – no-slip surface and no heat flux. The dash-dot curve is for the case of ΔT = 1.8 K, a no-slip surface and a radiative heat flux and is given for comparison. Note that under conditions of thermal insulation, $|\boldsymbol{v}_{av}|$ tends to zero at long times, whereas in the other simulations it tends to a positive constant value that is weakly influenced by the hydrodynamic boundary condition at the interface.

The radiative heat flux only becomes important at long times when the difference between the ambient temperature and that of the liquid is larger and, as the inset in Figure S.1 shows, the values of $|\boldsymbol{v}_{\mathrm{av}}|_{\mathrm{max}}$ for the simulations with no-slip conditions are nearly identical for no-flux and radiative flux conditions at the interface ($|\boldsymbol{v}_{\mathrm{av}}|_{\mathrm{max}}$ = 7.71 and 7.72x10^{-4} m·s^{-1}, respectively).

Figure S.8 presents results for $|\boldsymbol{v}_{\mathrm{av}}|$ for two simulations in which an approximation for the heat flux due to evaporation is included and for which ΔT = 2.3 K; they differ by the presence or absence of a radiative heat flux at the liquid|gas interface. The higher ΔT in these simulations leads to a higher maximum $|\boldsymbol{v}_{\mathrm{av}}|$ than in the cases illustrated in Figure S.1, $|\boldsymbol{v}_{\mathrm{av}}| \approx 1.01\text{x}10^{-3}$ m·s^{-1}. Moreover, according to our approximate model, evaporation leads to a considerably stronger outward flux at the interface than radiation and thus in this case, the average velocity at $t = t_{\mathrm{exp}}$ is also higher than in Figure S.1. The evaporative flux at the interface leads to $|v_{av}|_{t\,=\,t_{exp}} \approx$ 1.5x10^{-4} m·s^{-1}, whereas the combination of it and radiative flux yields 1.7x10^{-4} m·s^{-1}. As in the simulations without evaporation, the radiative heat flux only becomes important at long times, thus making the peak average velocities for the two cases illustrated in Figure S.8 identical to three significant digits.

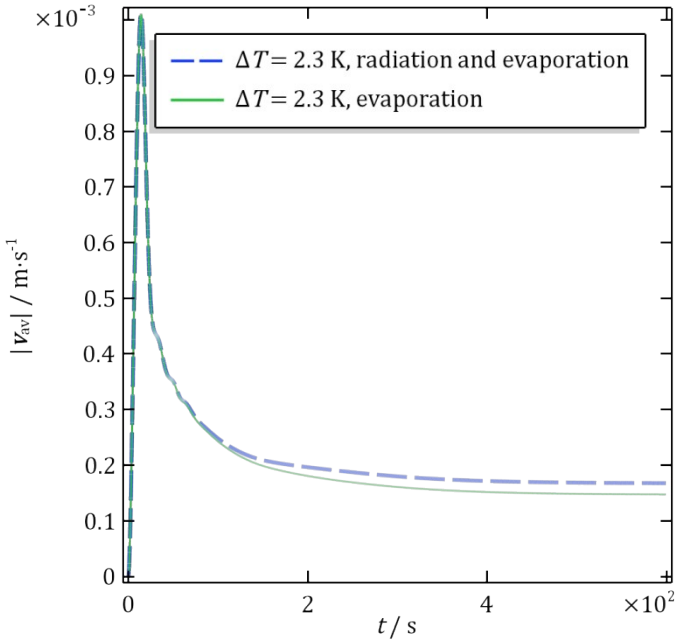

Figure S.8. Volume-averaged velocity magnitude for simulations with evaporation and a no-slip surface at ΔT = 2.3 K. The solid curve represents a model that includes only the heat flux due to evaporation, as given by eq. (9) in the main text, while the dashed takes the radiative heat flux (8) into account as well. Notice that the peak velocity is considerably higher than in Figure S.7 as a consequence of the larger initial temperature difference; furthermore, the stationary flow driven by evaporation has $|\boldsymbol{v}_{\mathrm{av}}|$ more than twice as high as the one caused by radiation alone.

Section 8. Thermostat system comparison

The homemade thermostat system was first tested by changing the temperature of 10 mL H_2O from the room temperature to the one of study. Figure S.9 shows the temperature profiles of 10 mL H_2O increasing from 21.9°C to 25.0°C (Figure S.9A) and from 22.6°C to 35°C (Figure S.9B) by using the homemade thermostat system (red curves) and the standard water bath (black curves). It can be seen that it took around 5 min for the homemade system to increase the temperature of 10 mL solution from 21.9°C to 25.0°C (red curves in Figure S.9A) and 10 min from 22.6°C to 35°C with high accuracy of measurement (± 0.1°C). In contrast, for experiments with the conventional water bath, the thermostat took around 22 min to increase the temperature of the bath itself (1L of water) from 20°C to 25°C, and about 32 min from 25°C to 35°C, then 5 min to heat 10 mL solution from 21.9°C to 25.0°C and 3 min from 22.6°C to 35.0°C. The control accuracy is ± 1°C. High efficiency and accuracy demonstrate that the homemade thermostat system has a good temperature control performance.

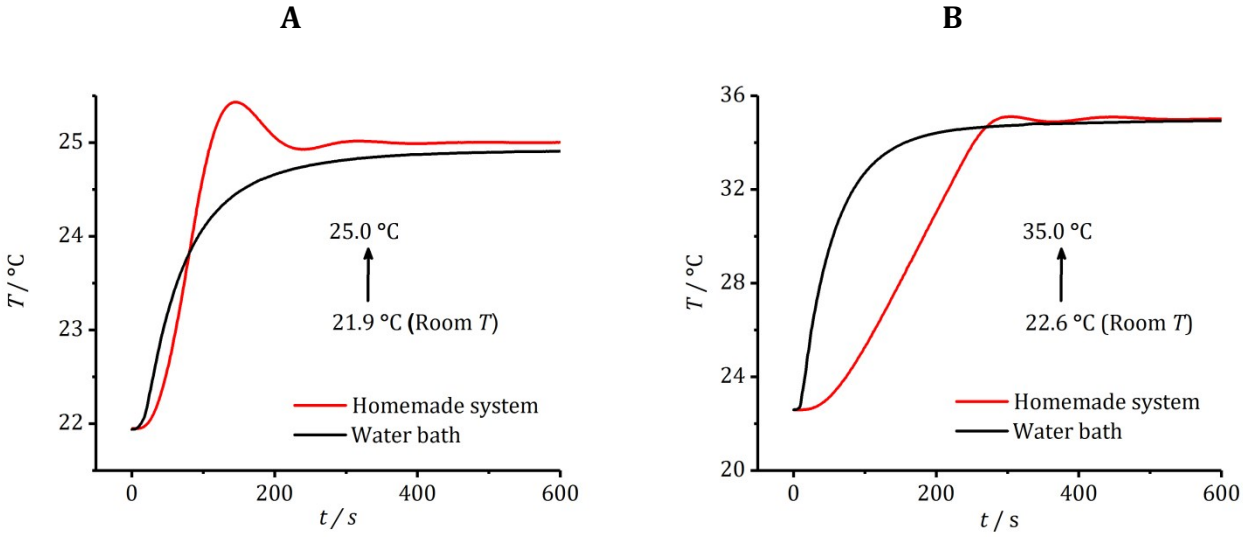

Figure S.9. Temperature profiles against time for the temperature of 10 mL H_2O increasing from room temperature 21.9°C to 25.0°C (**A**) and from 22.6°C to 35.0°C (**B**) in the homemade system (red curves) and the conventional water bath (black curves).

References

1. V. G. Levich, *Physicochemical Hydrodynamics*, Prentice-Hall, Inc., Englewood Cliffs, N.J., 1962.
2. H. Hu and R. G. Larson, *Langmuir*, 2005, **21**, 3972-3980.
3. J. R. Keller and T. L. Bergman, *J. Heat Transfer*, 1990, **112**, 363-369.
4. G. S. Kell, *J. Chem. Eng. Data*, 1975, **20**, 97-105.
5. J. Kestin, M. Sokolov and W. A. Wakeham, *J. Phys. Chem. Ref. Data*, 1978, **7**, 941-948.
6. C. A. Nieto de Castro, S. F. Y. Li, A. Nagashima, R. D. Trengove and W. A. Wakeham, *J. Phys. Chem. Ref. Data*, 1986, **15**, 1073-1086.
7. R. Cini, G. Loglio and A. Ficalbi, *J. Colloid Interface Sci.*, 1972, **41**, 287-297.